

Modeling Steady-State Experiments with a Scanning Electrochemical Microscope Involving Several Independent Diffusing Species Using the Boundary Element Method

Oleg Sklyar,[†] Markus Träuble, Chuan Zhao, and Gunther Wittstock*

Carl von Ossietzky University Oldenburg, Department of Pure and Applied Chemistry and
Institute of Chemistry and Biology of the Marine Environment, D-26111 Oldenburg, Germany

Received: April 28, 2006; In Final Form: June 14, 2006

The BEM algorithm developed earlier for steady-state experiments in the scanning electrochemical microscopy (SECM) feedback mode has been expanded to allow for the treatment of more than one independently diffusing species. This allows the treatment of substrate-generation/tip-collection SECM experiments. The simulations revealed the interrelation of sample layout, local kinetics, imaging conditions, and the quality of the obtained SECM images. Resolution in the SECM SG/TC images has been evaluated, and it depends on several factors. For most practical situations, the resolution is limited by the diffusion profiles of the sample. When a dissolved compound is converted at the sample (e.g., oxygen reduction or enzymatic reaction at the sample), the working distance should be significantly larger than in SECM feedback experiments (ca. $3 r_T$ for $RG = 5$) in order to avoid diffusional shielding of the active regions on the sample by the UME body. The resolution ability also depends on the kinetics of the active regions. The best resolution can be expected if all the active regions cause the same flux. In one simulated example, which might mimic a possible scenario of a low-density protein array, considerable compromises in the resolving power, were noted when the flux from two neighboring spots differs by more than a factor of 2.

I. Introduction

Scanning electrochemical microscopy (SECM) has become an invaluable tool for analyzing local reactivities at solid–liquid, liquid–liquid, and liquid–gas interfaces.^{1–5} In SECM experiments, a Faradaic current, i_T , is measured at an ultramicroelectrode (UME) used as local probe. The current is controlled by the diffusional flux of oxidizable/reducible species toward the active area of the UME, which in turn is influenced by the geometries of the sample and the probe as well as the interfacial reactivity of the sample. While lateral resolution in routine SECM experiments does not reach the resolution easily achieved with scanning force microscopy or scanning tunneling microscopy, the importance of SECM results from its unique ability to analyze local chemical fluxes. This analysis can provide quantitative results because the mass transport between the scanning probe, the UME, and the sample under investigation is usually controlled by diffusion, which is a theoretically well understood phenomena that can be described by continuum models with sufficient accuracy under the prevailing experimental conditions. The local kinetic analysis benefits further from the steady-state nature of most SECM experiments and small overall currents. The latter minimizes typical error sources such as limited instrumental rise time and iR drop due to uncompensated resistance that have to be considered in other common electrochemical methods.

Since the inception of SECM, the experimental work has been accompanied by digital simulations.^{6–13} Simulations are carried out for different parameter sets that include kinetic quantities.

The kinetic constants are then determined as those that lead to the closest match of the simulated dataset with the experimental results. Such numerical simulations, as a basis for a quantitative interpretation of SECM, have been performed using different simulation techniques. Most simulations have been performed by finite difference methods (FDM).^{8,14,15} Finite elements simulations were initially used and are currently revisited.^{6,13,16} Because of the difficulties in execution of the FDM in three-dimensional space (3D) coordinates,¹⁵ most calculations deal with axisymmetric situations and greatly simplified geometries that allow the calculations to cast a two-dimensional (2D) simulation problem. Fulian et al. introduced the use of the boundary element method (BEM) for the numerical solution of SECM problems.^{17–22} The initial idea has been expanded by a series of contributions from this laboratory.^{11,23–25} The extensions comprise the use of true 3D coordinates which allows us address important questions such as resolution, effect of distance control systems on SECM response, and response of SECM probes with arbitrary geometry.^{11,23} The accuracy of the simulations was enhanced to the level achieved before by FDM by using the exterior formulation of the Laplace problem instead of the interior formulation that must be used for FDM and FEM, but was also selected by Fulian et al. for their BEM work.¹¹ The possibility to simulate experiments with finite kinetics was demonstrated.²⁴ The stability of the solution was enhanced by casting all boundary conditions into a linear combination of flux and concentration values (Robin–Couchy) instead of allowing the coexistence of boundary elements with specified constant flux (Neuman-type) and with specified constant concentration (Dirichlet-type) on a single enclosed object.²⁴

With these extensions the BEM can easily be applied to any SECM experiment in the feedback mode under steady state conditions (Figure 1a). Such problems are typically treated by

* Corresponding author fax: (+49–441) 7893979; e-mail: gunther.wittstock@uni-oldenburg.de.

[†] Present address: European Bioinformatics Institute, Wellcome Trust Genome Campus, Hinxton, Cambridge, CB10 1SD, United Kingdom.

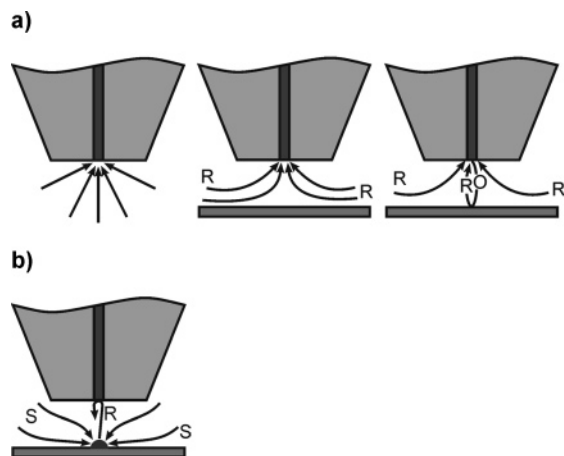


Figure 1. (a) Schematic drawing of the SECM feedback mode with the reduced form R of a redox mediator provided in the bulk phase; (b) Schematic drawing of the SECM SG/TC experiment where a nonredox compound S is provided in the bulk phase. This compound S is converted at a microscopic region at the sample to a redoxactive compound R that is detected by the UME.

considering the mass conservation of the mediator couple $R \rightarrow O + n e^-$ and assuming the equality of the diffusion coefficients $D_O = D_R = D$. Under such conditions, the concentrations of both redox forms, c_O and c_R , are coupled $c_O + c_R = c^*$, where c^* is the bulk concentration of the mediator. The feedback mode is also the working mode to which most of the other simulations refer. This may be influenced by the, somewhat pessimistic, expectation expressed by Bard et al. with regard to the applicability of the generation–collection mode (the alternative working mode).²⁶ Meanwhile, it has turned out that the generation–collection (GC) mode, and specifically, the sample-generation/tip-collection mode (SG/TC) is invaluable for investigations in a number of technologically important applications, where the feedback mode cannot be applied (Figure 1b). Examples include the mass transport through skin and pores,^{27,28} the investigations of immobilized enzymes that are not oxidoreductases,^{29–32} immunoassays on chips,^{33,34} evaluation of cultivated cells,^{35–41} and local defects in passivation layers of valve metals.^{42–46} Possibilities for quantification exist if the reaction on the sample can be switched on and off and a current-time trace is recorded at the UME positioned at a defined distance from the sample,^{47,48} or if the active region on the sample is a microstructure itself, which forms a steady-state hemispherical diffusion field.^{28,49} The latter situation dominates the published applications. Quantification can be based on suggestion from White et al. that assumes the UME as a passive probe for the diffusion field of a microscopic generator at the sample.^{28,49} The UME behaves approximately as a passive probe (i.e., a sensor that does not consume the analyte) if the conversion at the UME does not disturb the local diffusion field above the sample significantly. Considerable doubts are appropriate, to which extent this assumption is indeed fulfilled in all studies. For locally immobilized enzymes or cells there is an even other problem nicely illustrated in Figure 5 of ref 50. The presence of the UME above the active region of the sample hinders the diffusion of the enzyme substrate toward the active region of the sample (Figure 1b). We often tried to avoid this problem by providing the enzyme substrate in much larger concentrations than the Michaelis–Menten constant K_M of the enzyme. Because of limited solubilities or the impossibility of investigating the behavior quantitatively under conditions of small substrate supply (e.g., important for studies on living cells),

such an approach has severe limitations with regard to expanding it to new problems.

In this study, we describe the extension of the exterior BEM formalism to treat more than one independent concentration variable in a true 3D space. This is applied to a simple SG/TC experiment with the enzyme galactosidase. This enzyme catalyzes the hydrolysis of *p*-aminophenyl- β -D-galactopyranoside (PAPG, species 1) to *p*-aminophenol (PAP, species 2). PAP is detected amperometrically at the UME and converted to *p*-quinone imine. FDM simulations of axisymmetric 2D SECM systems with two independent concentrations have been reported before. Macpherson and Unwin modeled the SECM investigation of the dissolution kinetics of AgCl.⁵¹ Barker et al. reported on SECM investigations and corresponding modeling of transfer kinetics at liquid–liquid interfaces.^{52–54} The only GC mode simulation performed by Martin and Unwin using the FDM was restricted to electrochemical reactions at the UME and the sample.^{14,55,56} However, no simulations have been done for systems of immobilized enzymes in the GC mode so far. Besides limiting the discussion to approach curves, previous axisymmetric 2D modeling of SECM problems were not able to address such important questions as resolution under different experimental conditions.

II. Experimental and Simulation Details

Solution. Biotin-labeled β -galactosidase (catalog no. G5025, from *Escherichia coli*, 680 U mg⁻¹, one unit will hydrolyze 1.0 μ mole of *o*-nitrophenyl- β -D-galactoside per min at pH 7.3 at 37 °C), *p*-aminophenyl- β -D-galactopyranoside (PAPG) and *p*-aminophenol (PAP) were purchased from Sigma (Sigma-Aldrich Chemie GmbH, Schnellendorf, Germany). Streptavidin-coated M-280 Dynabeads (2.8 μ m diameter) were from Dynal Inc. (Great Neck, NY) as a monodisperse suspension of 6.7×10^8 beads mL⁻¹ and 7×10^5 Streptavidin molecules per bead. K₂HPO₄, NaH₂PO₄, MgCl₂, KCl (Fluka, Deisenhofen, Germany) and Tween 20 (Sigma, Steinheim Germany) were used as received. The substrate solution contained 2×10^{-6} mol cm⁻³ PAPG in 1.0×10^{-4} mol cm⁻³ phosphate buffer (pH 7.0) containing 1.0×10^{-5} mol cm⁻³ MgCl₂. All chemicals used were of analytical reagent grade. Deionized water was used throughout.

Instruments. The SECM images were taken on a home-built instrument based on a positioning system from Scientific Precision Instruments (Oppenheim, Germany). All experiments were carried out with a 25 μ m diameter Pt UME. A Pt wire as auxiliary electrode and a Ag|AgCl|3 M KCl reference electrode, to which all potentials are referred, completed the electrochemical cell. For all SECM experiments, a monopotentiostat μ -P3 (M. Schramm, Heinrich Heine University, Düsseldorf, Germany) was used.

Procedures. Ten microliter streptavidin-coated M-280 microbead suspension was mixed with 100 μ L of biotinylated β -galactosidase diluted to 40 μ g mL⁻¹ in 0.1 M phosphate buffer solution (pH 7.0). The mixture was agitated gently on a plate-shaker for 30 min. Supernatant solution was removed in three rinses with 100 μ L phosphate buffer containing 0.5% (v/v) Tween 20. Between rinses a magnet pressed against the wall of the tube was used to hold the beads. Finally, 150 μ L phosphate buffer was added to resuspend the beads in the tube. The final concentration of beads in the test tube was 4.7×10^7 beads mL⁻¹. The modified microbeads were then deposited as microspots on the insulating surface according to the previously described procedure.³⁰ Microscope glass slides (ca. 76 \times 26 mm², Carl Roth GmbH, Karlsruhe, Germany) were used as

support and were covered by stretched Parafilm (American National Can, Chicago, IL) to obtain a hydrophobic surface. For each microspot, 1 μL of the bead suspension was taken up in a variable volume pipet (Eppendorf Research, 0.1–2.5 μL , Eppendorf GmbH, Hamburg, Germany). The tip of the micropipet was mounted in the electrode holder of the SECM translation stage and a 0.7 μL drop was extruded and held 500 μm above the support surface. A permanent magnet was placed below the support and within 30 s all the beads were pulled to the bottom of the drop. Then the volume of the hanging drop was reduced to 0.3 μL before bringing it slowly in contact with the hydrophobic surface. After contact, the tip was retracted and because of the hydrophobicity of surface, the drop did not wet the surface but remained on the retracting micropipet leaving behind only a mound of beads on the slide.

The SECM images were obtained in SG/TC mode by translating the UME at a vertical distance of 45 μm above bead microspots with a translation speed of 10 $\mu\text{m s}^{-1}$ and a UME potential, $E_T = 350$ mV to detect the product *p*-aminophenol. The in-house software MIRA was used to process and analyze the data.⁵⁷

Simulation Tools. Simulations with the BEM were performed with an in-house developed software¹¹ written in C++ on a Linux-PC with a 2 GHz processor and 512 MB of RAM. The average computation time was approximately 1–2 min for a single geometric configuration of approximately 3750 mesh elements and required 320 MB of memory. A whole image consisting of 50×50 data points could be calculated in 29 h. The following algorithms were used in the overall BEM setup: the Gauss–Legendre 13-point quadrature rules for numerical integration and analytical two-dimensional surface integration (Appendix A), a biconjugate gradient preconditioned method (BCGPC) for solution of dense linear systems and the Delaunay triangulation for composing the mesh. A separate geometry editor was created and used for mesh development and assignment of boundary conditions to mesh elements.

III. Results and Discussion

Theory. The currently available BEM simulations have enabled the treatment of truly 3D problems already, but have been restricted to one independent variable for concentration only.^{11,23,24,58} The experiment shown in Figure 1b requires, in order to be modeled, a treatment of two independent local concentrations $c_S(\mathbf{r})$ and $c_R(\mathbf{r})$, where $c_X(\mathbf{r})$ denotes the concentration of species X at the point \mathbf{r} (The mathematical literature calls such problems multidimensional problems, thereby referring “dimension” to one kind of independent local variable. To avoid confusion with the space coordinates, which are considered as “dimension” by most experimenters, we avoid this terminology in the context of SECM). At the sample, S is enzymatically converted to R. (Other educts such as H_2O are not considered if their concentration is in large excess. Other products of the enzymatic reaction that are not redoxactive, e.g., galactose do not need to be treated to calculate the SECM signal.)



This conversion is assumed to follow Michaelis–Menten kinetics and proceeds according to a heterogeneous rate law [$\text{mol cm}^{-2} \text{s}^{-1}$], because all the enzyme is immobilized on the surface only.

$$f_{[\text{R}]} = -f_{[\text{S}]} = \frac{k_{\text{cat}} \Gamma_{\text{enz}} c_S(\mathbf{r}_{\text{surface}})}{K_M + c_S(\mathbf{r}_{\text{surface}})} \quad (2)$$

where f is the heterogeneous reaction rate for the consumption of R or the formation of S, k_{cat} is the turnover number, Γ_{enz} is the surface concentration of the enzyme and K_M is the Michaelis–Menten constant. Provided that the sample region, at which the conversion occurs, is a microscopic region itself, steady-state concentrations for both, S and R, will be established in the solution. At the UME, species R is oxidized to O under diffusion-controlled conditions.



To solve the SECM problem, a system of Laplace eqs 4 and 5

$$\frac{\partial c_S(\mathbf{r}, t)}{\partial t} = 0 = \nabla^2 c_S(\mathbf{r}), \quad \mathbf{r} \in V \quad (4)$$

$$\frac{\partial c_R(\mathbf{r}, t)}{\partial t} = 0 = \nabla^2 c_R(\mathbf{r}), \quad \mathbf{r} \in V \quad (5)$$

has to be solved. ∇^2 is the Laplace operator and V is the simulation domain. The BEM proceeds by transforming eqs 4 and 5 into their integral representation at the domain boundary Γ according to Green’s second identity and its further discretization at triangular boundary elements,¹¹

$$\frac{1}{2} c_S(\mathbf{r}_i) = \sum_{j=1}^N \frac{\partial c_S(\mathbf{r}_j)}{\partial \mathbf{n}_j} \iint_{\Gamma_j} G(\mathbf{r}, \mathbf{r}_i) d\Gamma - \sum_{j=1}^N c_S(\mathbf{r}_j) \iint_{\Gamma_j} \frac{\partial G(\mathbf{r}, \mathbf{r}_i)}{\partial \mathbf{n}_j} d\Gamma \quad (6)$$

$$\frac{1}{2} c_R(\mathbf{r}_i) = \sum_{j=1}^N \frac{\partial c_R(\mathbf{r}_j)}{\partial \mathbf{n}_j} \iint_{\Gamma_j} G(\mathbf{r}, \mathbf{r}_i) d\Gamma - \sum_{j=1}^N c_R(\mathbf{r}_j) \iint_{\Gamma_j} \frac{\partial G(\mathbf{r}, \mathbf{r}_i)}{\partial \mathbf{n}_j} d\Gamma \quad (7)$$

where for one specific element i , the sum over all N boundary elements indexed by j is taken with values of concentrations $c_X(\mathbf{r})$, the fluxes $\partial c_X(\mathbf{r})/\partial \mathbf{n}_j$ ($X = \text{S or R}$). $G(\mathbf{r}_i, \mathbf{r}_j) = (4\pi|\mathbf{r}_i - \mathbf{r}_j|)^{-1}$ is the standard Green function for the Laplace equation calculated from the absolute distance $|\mathbf{r}_i - \mathbf{r}_j|$ between the elements i and j . N linear equations for S (eq 6) and the N linear equations for R (eq 7) are bound together by boundary conditions that include the other concentration, e.g., the formation rate for R at enzymatically active sample regions depends on $c_S(\mathbf{r})$ (eq 2). For n_{spec} independent concentration variables, a system of $n_{\text{spec}} N$ equations with $n_{\text{spec}} N$ concentration values and $n_{\text{spec}} N$ flux values has to be solved, from which $n_{\text{spec}} N$ values are unknown. This system of equation can be written in matrix form as

$$\mathbf{G} \times \mathbf{h} - \mathbf{H} \times \mathbf{c} = 0 \quad (8)$$

For definition and calculation of the matrix elements see Appendix A.

Representation of Different Boundary Conditions. Heterogeneous reactions are represented as boundary conditions in a BEM setup. To assign boundary conditions flexibly even for complex SECM experiments, our approach uses two

programs. A stand-alone application, BEMEditor, constructs objects for the UME and the sample and provides different routines for meshing. Meshing can be done automatically and can be refined by user input. Each mesh element is assigned a tag, that corresponds to a specific boundary condition. In the simulation of a simple GC experiment, three different tags would be used (insulating and inert parts of the UME and sample, active electrode area of the UME, and the enzymatically active region). In a second program, BEMSolver, each tag is associated with a boundary condition matrix (BC). For a system with two independent concentration variables ($n_{\text{spec}} = 2$), the BC would look like the following:

$$BC = \begin{bmatrix} b_{0,0} & b_{0,1} \\ b_{1,0} & b_{1,1} \end{bmatrix} \begin{bmatrix} a_0 \\ a_1 \end{bmatrix} \quad (9)$$

Fluxes in the direction of the surface normal vector are given for every boundary element by the following expression:

$$\frac{\partial c_i}{\partial \mathbf{n}} = a_i + \sum_{j=0}^{n_{\text{spec}}-1} b_{i,j} c_j \quad (10)$$

To use the exterior formulation of the Laplace problem, one has to operate by variables (concentrations), whose bulk values are initially zero or introduce variable substitutions (transformed concentration quantities) to meet these requirement. For modeling the SG/TC mode with the enzyme galactosidase, the concentrations of PAPG and PAP have to be considered. The concentration of PAP is initially zero in the bulk phase and can be used directly for the simulation, i.e., $c_1 = [\text{PAP}]$. The concentration of PAPG is not zero in the bulk phase since this is the enzyme substrate. We obtain an equivalent concentration quantity by the substitution $c_0 = [\text{PAPG}]^* - [\text{PAPG}]$ where the star denotes the bulk concentration. Thus the concentration vector used for the simulation is

$$\begin{bmatrix} c_0 \\ c_1 \end{bmatrix} = \begin{bmatrix} [\text{PAPG}]^* - [\text{PAPG}] \\ [\text{PAP}] \end{bmatrix} \quad (11)$$

The boundary condition linking c_0 and c_1 can be derived from the consumption rate of PAPG and the formation rate of PAP with $k_1' = k_{\text{cat}} \Gamma_{\text{enz}}/K_M$ as the pseudo first-order rate constant of the enzymatic reactions for $[\text{PAPG}] < K_M$.

$$\frac{\partial [\text{PAPG}]}{\partial \mathbf{n}} = -\frac{k_1'}{D_{\text{PAPG}}} [\text{PAPG}] = -\frac{k_1'}{D_0} (c_0^* - c_0) = -\frac{\partial c_0}{\partial \mathbf{n}} \quad (12)$$

Because the formation rate of PAP is the sign-inverted value of the consumption, the boundary condition is

$$\frac{\partial [\text{PAP}]}{\partial \mathbf{n}} = \frac{k_1'}{D_{\text{PAP}}} [\text{PAPG}] = \frac{k_1'}{D_1} (c_0^* - c_0) = \frac{\partial c_1}{\partial \mathbf{n}} \quad (13)$$

For this example the BC matrix looks like

$$BC = \begin{bmatrix} -k_1'/D_0 & 0 \\ -k_1'/D_1 & 0 \end{bmatrix} \begin{bmatrix} -k_1'c_0^*/D_0 \\ -k_1'c_0^*/D_1 \end{bmatrix} \quad (14)$$

For $[\text{PAPG}] \gg K_M$, a constant formation rate of PAP is observed. With $k_1' = k_{\text{cat}} \Gamma_{\text{enz}}$ the BC matrix is in this case

$$BC = \begin{bmatrix} 0 & 0 \\ 0 & 0 \end{bmatrix} \begin{bmatrix} -k_1'/D_0 \\ -k_1'/D_1 \end{bmatrix} \quad (15)$$

For the insulating and inert parts of the probe and the sample the BC is

$$BC = \begin{bmatrix} 0 & 0 \\ 0 & 0 \end{bmatrix} \begin{bmatrix} 0 \\ 0 \end{bmatrix} \quad (16)$$

For the active electrode surface of the UME, a diffusion-controlled reaction shall be modeled. This is achieved by setting the first-order rate constant k_2 to a high value (100). We did not note detectable differences if k_2 assumes values larger than 10. Selecting any value larger than 10 is equivalent to a diffusion-controlled reaction and avoids the numerical difficulties if different boundary condition types (Neumann and Robin) are present on one enclosed object.

$$BC = \begin{bmatrix} 0 & 0 \\ 0 & k_2/D_1 \end{bmatrix} \begin{bmatrix} 0 \\ 0 \end{bmatrix} \quad (17)$$

Comparison to Experimental Results. To compare the simulation approach to a SG/TC experiment, we selected an experiment that is well established in our laboratory. It uses paramagnetic microbeads of 2.8 μm diameter, that are surface-modified with the enzyme galactosidase using biotin-streptavidin chemistry.²⁹ The beads are confined into a mound within a microscopic droplet that is placed onto a hydrophobic surface in an external magnetic field.³⁰ The size of the bead mound is determined by the concentration of the beads in the bead suspension. The activity of the immobilized galactosidase is imaged in the SG/TC mode using PAPG as the substrate. The enzymes forms PAP, which is detected amperometrically by the UME (Figure 2b). The simulated image in Figure 2d was obtained by taking the geometric parameters from the experiment in Figure 2a and b. The height of the bead spot was taken as 15 μm . This value was shown to be representative for this kind of deposition.⁵⁹ The bead mound was represented as a smooth spherical cap, where all the enzyme activity is located at the outer surface, with the surface concentration of the enzyme corresponding to 50% saturation of the available avidin binding sites (7×10^5 sites per bead).⁶⁰ Geometrical features of individual beads were not considered. Such averaging is possible because the roughness of the bead-agglomeration surface can be neglected on the scale of the imaging distance $d = 40 \mu\text{m}$ and of the size of the bead mound of 150–300 μm . If concentration distributions between individual beads are of interest, the results for the average fluxes of different components can be used for the low-scale simulations on individual beads, in which the geometry of every bead is considered. This kind of simulations is, however, out of scope for this work. Several simulations have been preformed for different bulk concentrations of PAPG. The best agreement of the simulated signal with the experimentally measured one was found for an assumed concentration $[\text{PAPG}]^* = 5.0 \times 10^{-7} \text{ mol cm}^{-3}$. This assumed value is smaller than the experimentally used value of $[\text{PAPG}]^* = 2.0 \times 10^{-6} \text{ mol cm}^{-3}$. There are two reasons which make it plausible that the experimental and simulated images agree despite the difference between $[\text{PAPG}]^*$ in the experiment and the simulation. The simulation assumes uniformly accessible enzymes, which is clearly not the case. Since the simulation treats the enzymatic reaction as a pseudo first-order reaction with respect to PAPG (eqs 12–14), this simplifying assumption may be balanced by assuming a slightly reduced $[\text{PAPG}]^*$. Second, it is seen from the Michaelis–Menten curve in Figure 3 (calculated from the simulation data of this numerical

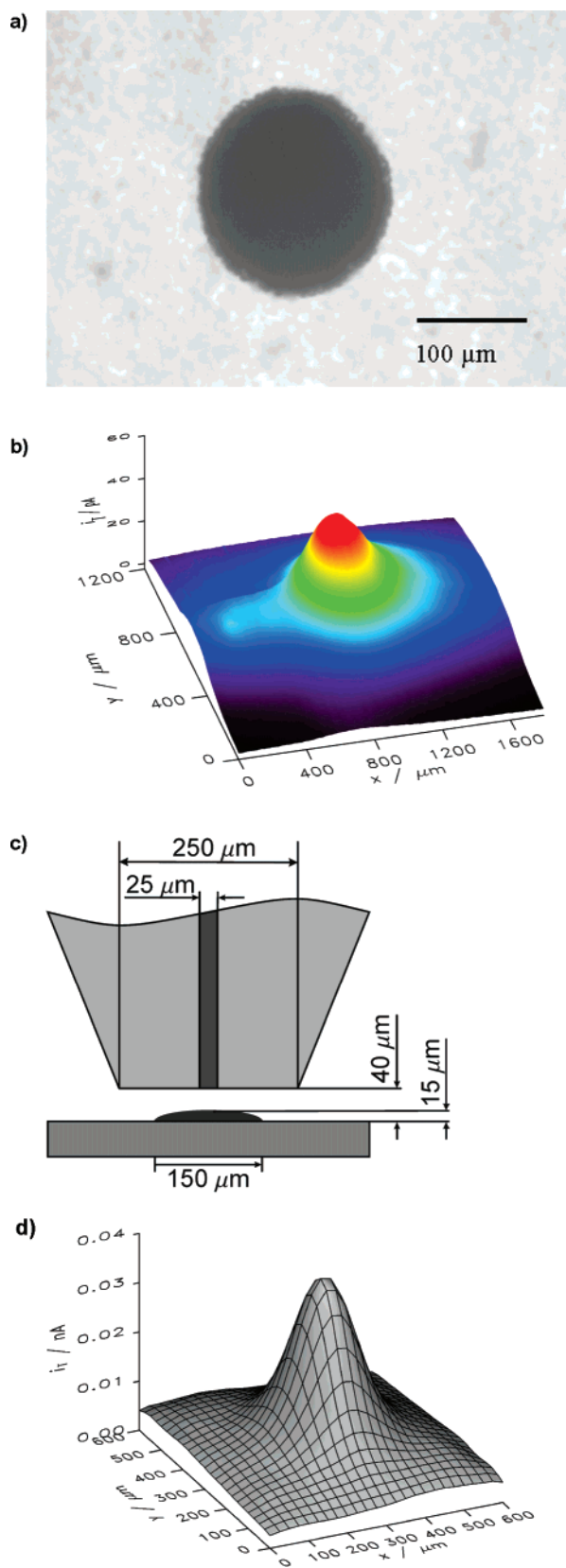


Figure 2. (a) Optical microphotograph of the bead mound; (b) experimental SG/TC image of PAP production from PAPG, experimental conditions $[PAPG] = 2.0 \times 10^{-6} \text{ mol cm}^{-3}$, $r_T = 12.5 \text{ μm}$, translation speed = 10 μm s^{-1} (c) Schematic of the geometric arrangement used in the simulation; (d) simulated image using the following kinetic parameters: $K_M = 1.79 \text{ mol cm}^{-3}$, $k_{cat}\Gamma_{enz} = 4.49 \times 10^{-12} \text{ mol cm}^{-2} \text{ s}^{-1}$ and $c_0^* = 5.0 \times 10^{-7} \text{ mol cm}^{-3}$.

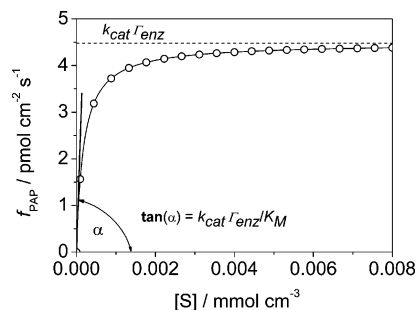


Figure 3. Michaelis-Menten curve for surface-immobilized galactosidase calculated by assuming $K_M = 1.79 \times 10^{-7} \text{ mol cm}^{-3}$ and $k_{cat}\Gamma_{enz} = 4.49 \times 10^{-12} \text{ mol cm}^{-2} \text{ s}^{-1}$; $f_{PAP} = k_{cat}\Gamma_{enz} [S] / (K_M + [S])$.

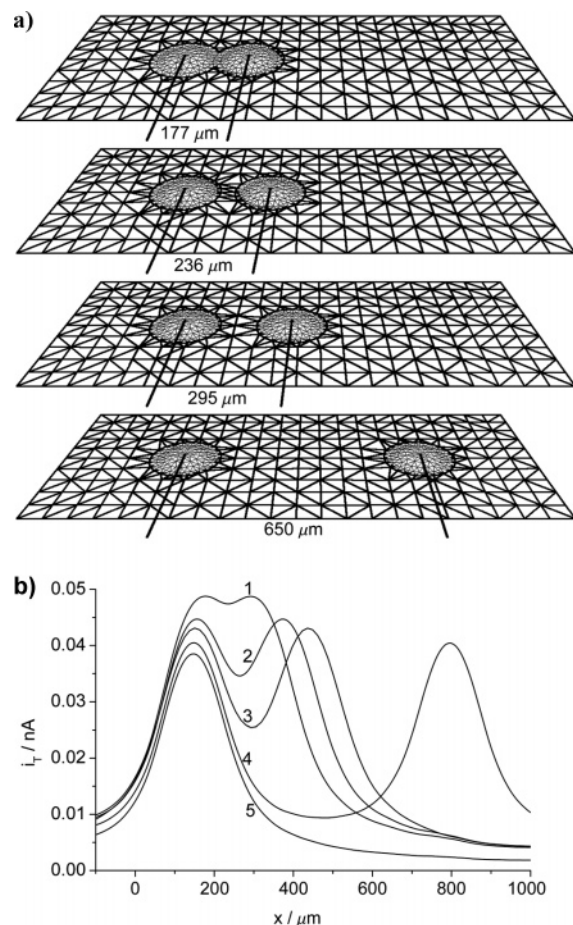


Figure 4. Simulation of SG/TC experiments for two bead mounds placed on the same support. Each bead mound has parameters as those shown in Figure 2c. (a) Layout of the spots; midpoint-midpoint distances are (1) 177 μm , (2) 236 μm , (3) 295 μm , (4) 650 μm ; (b) corresponding line scans over the center of the bead spots for layouts 1–4. Assumed parameters are $[PAPG]^* = 5.0 \times 10^{-7} \text{ mol cm}^{-3}$, $r_T = 12.4 \text{ μm}$, spot diameter = 150 μm ; spot height in the center = 1.5 μm , $K_M = 1.79 \times 10^{-7} \text{ mol cm}^{-3}$ and $k_{cat}\Gamma_{enz} = 4.49 \times 10^{-12} \text{ mol cm}^{-2} \text{ s}^{-1}$.

experiment) that the difference in the PAP flux when changing $[PAPG]^*$ from 2.0 to $5.0 \times 10^{-7} \text{ mol cm}^{-3}$ is at the level of 20%, fixing the uncertainty of calculations at this level. Furthermore, the concentration of PAPG will be reduced at the surface of the bead mound, however, the reduction of the local $[PAPG]$ occurs to a different extent. Since a concentration of $2.0 \times 10^{-6} \text{ mol cm}^{-3}$ PAPG falls in the transition region of first to zero order kinetics of galactosidase (Figure 3), a more precise calculation must assign different types of boundary conditions to different sample regions. This is currently not

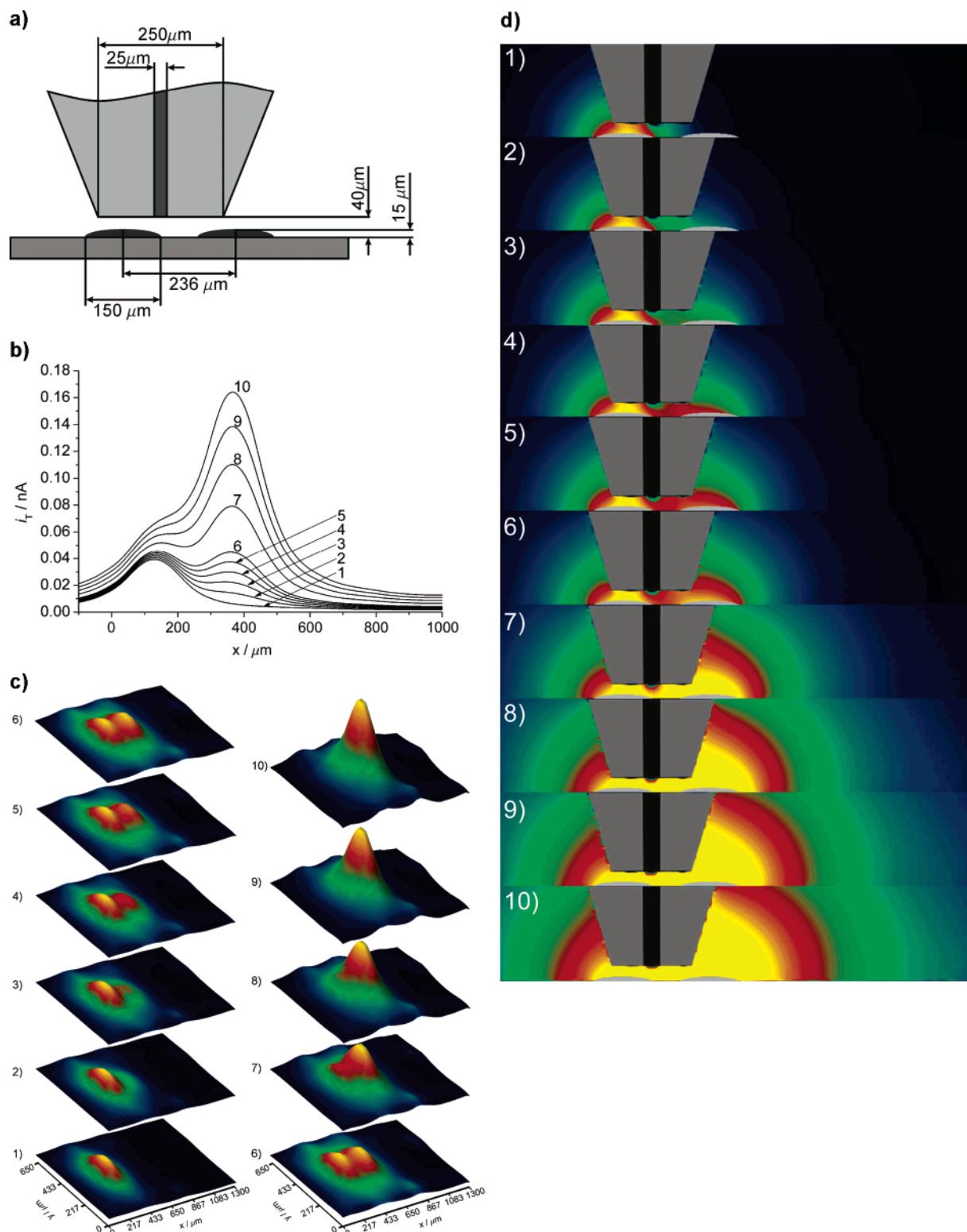


Figure 5. Simulation of images of two bead mound of identical shape but with different enzyme loading. (a) geometric layout of the simulation. Each spot has geometric parameters as in Figure 2c. The value for K_M was $1.79 \times 10^{-7} \text{ mol cm}^{-3}$. The left spot had $(k_{\text{cat}}\Gamma_{\text{enz}})_{\text{left}} = 4.49 \times 10^{-12} \text{ mol cm}^{-2} \text{ s}^{-1}$ throughout the series of simulation. The value of $(k_{\text{cat}}\Gamma_{\text{enz}})_{\text{right}}$ for the right spot was in multiples of $(k_{\text{cat}}\Gamma_{\text{enz}})_{\text{left}}$ (1) 0, (2) 0.2, (3) 0.4, (4) 0.6, (5) 0.8, (6) 1, (7) 2, (8) 3, (9) 4, (10) 5. (b) Line scans over the center of the bead spots. The numbers at each trace refer to the simulation setup described above. (c) 3D representation of the entire images for the setups 1–10. (d) local PAP concentration when the UME is placed above the right edge of the left spot for the simulation setups 1–10.

possible. The values assumed for the K_M and the $k_{\text{cat}}\Gamma_{\text{enz}}$ are reasonable assumptions in the light of previous SG/TC experiments.

In conclusion we are able to simulate, at least semiquantitatively, SG/TC experiments of arbitrary geometries and rather complex kinetics without the need to assume the UME as a

noninteracting probe. We can also consider the effect of the PAPG flux shielding by the UME body.

Resolution of SG/TC Experiments. While the resolving power in SECM experiments is primarily a function of the UME electrode, this statement is not necessarily true for the SG/TC mode. Many evaluations assumed that the probe is passive, i.e.,

the presence of the probe does not disturb the concentration profile formed in the vicinity of the generator at the sample.^{28,44} This condition is approached, when the UME is considerably smaller than the active region on the sample. In such a case, the resolution exclusively depends on the properties of the sample. In real experiments, this condition may, however, not be perfectly met and the UME may disturb the concentration profile above the sample by local consumption of a species and by blocking the diffusion of educts and products of the sample reaction. We used the simulation approach outlined above to simulate images in which two bead spots, as shown in Figure 2c, are placed at different distances on the same support. Figure 4 shows line scans over the center of the bead spots. In agreement with experimental results by several groups,^{44,50,61,62} it is shown that the presence of two overlapping signals is evident at very small lateral spacings of the spots. For a qualitative microscopic interpretation, this may lead already to very valuable insights, if the presence and the spacings of active regions on a sample is of primary interest. However, very large lateral distances are required if baseline-resolved signals are required for quantitative evaluations of individual active regions. The peak heights between line scan 1 in Figure 4 (almost complete overlapping peaks) and line scan 4 (almost baseline resolved) differ, at most, by 20% from the value of the isolated spot (line scan 5). If such an accuracy level is sufficient for a semiquantitative understanding, even almost fully overlapping peaks may be analyzed using the approximations of a noninteracting probe.

Resolution of Spots with Different Activity. Another factor that influences the resolving power of two active regions is the kinetics at each active region that may lead to different fluxes. This situation has importance for instance in readouts of biochips, where spots of low intensity ought to be detected in the presence of much more active spots in their vicinity. This problem was investigated by a series of simulations using two active regions of identical geometry (shown in Figure 2c) but with different kinetics. The distance between midpoints was selected as 236 μm , a value that led to two clearly identifiable, yet overlapping, signals in Figure 4b. The simulation results are shown in Figure 5. The simulations give ground for some very interesting and important conclusions. The presence of two active regions can only be seen at the given spacing in the images in Figure 5b, if the value of $k_{\text{cat}}\Gamma_{\text{enz}}$ of the two spots differ no more than by a factor of 2. The line scans over the centers of both bead mounds in Figure 5c confirm and summarize that result. If the enzyme loading differs by more than a factor two, larger spacings are required to allow the identification of individual signals. This conclusion is important for a number of applications including electrochemical detection of biochips with enzyme labels, identification of corrosion pits or precursors on passivated metals, or mass transport through porous membranes with nonuniform pore size.

Once the BEM equations are solved, fluxes and concentration at the boundary of the simulation domain are known. With these values, the local steady-state concentration inside the volume can be calculated using eq 18.

$$\theta c_X(\mathbf{r}_i) = \sum_{j=1}^N \frac{\partial c_X(\mathbf{r}_j)}{\partial \mathbf{n}_j} \iint_{\Gamma_j} G(\mathbf{r}, \mathbf{r}_i) d\Gamma - \sum_{j=1}^N c_X(\mathbf{r}_j) \iint_{\Gamma_j} \frac{\partial G(\mathbf{r}, \mathbf{r})}{\partial \mathbf{n}_j} d\Gamma \quad (18)$$

Please note that eq 18 differs from eqs 6 and 7 in the geometric factor θ preceding the concentration of a species X on the left side. It is $\theta = 1$ for internal points and $\theta = 1/2$ for points on

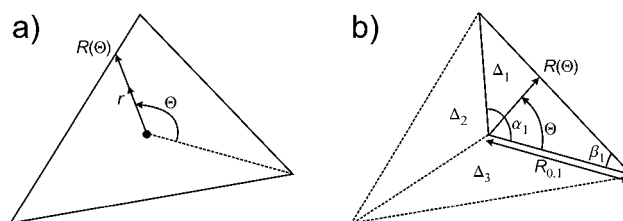


Figure 6. Analytical integration for matrix elements G_{ii} . (a) Radial coordinates within the boundary element; (b) division of the element into three triangles for integration over θ .

the boundary. The resulting values are shown in Figure 5d. The images represent the concentration distribution of PAP in the xz plane. The x and y coordinates are identical to those used to calculate the line scans in Figure 5c. The concentration distributions in Figure 5d illustrate the situation when the UME is located right over the right edge of the left spot. This is the situation, which is important for resolving the two features. Two observations can be made: First, the diffusion field over the sample is comparatively little disturbed if the working distance of the UME in the SG/TC mode is not too small (40 μm in the simulation). This justifies the treatment of the signals by the simplifying assumption of a noninteracting probe, which has been used in a number of applications.^{28,29,44,63} Second, if the kinetics at the active regions differ more than by a factor of ca. 2, the overlapping diffusion layers will be dominated by the flux from only one spot, which is in line with the simulated images and line scans.

IV. Conclusion

The BEM algorithm introduced earlier for the calculation of steady-state SECM experiments in 3D space has been expanded to allow for the treatment of more than one independently diffusing species. This allows the treatment of SG/TC SECM experiments which have a high practical relevance due to their application for imaging immobilized enzymes and catalysts, cells and local reactions at passivated metals, and membrane transport. The simulation could reveal the interrelation of sample layout, local kinetics, imaging conditions, and the quality of the obtained SECM images. Resolution in the SG/TC images depends on several factors. For most practical situations, the resolution is limited by the diffusion profiles of the sample. When a dissolved compound is converted at the sample (e.g., oxygen reduction or enzymatic reaction at the sample), the working distance should be significantly larger than in SECM feedback experiments (ca. 3 r_T for $RG = 5$) in order to avoid diffusional shielding of the active regions on the sample by the UME body. For enzymatic reactions, this problem can be avoided if substrate concentrations much larger than the K_M value can be used. Due to solubility limitations, this is, however, not always possible, and in those cases an increase of the working distance or a decrease of the RG have to be used. The resolution ability also depends on the kinetics of the active regions. The best resolution can be expected if all the active regions cause the same flux. In the considered example, which might mimic a possible scenario of a low-density protein array, considerable compromises in the resolving power were noted, when the flux from two neighboring spots differs by more than a factor of 2.

Acknowledgment. The work was supported by Deutsche Forschungsgemeinschaft under grant Wi 1617/6 and Wi 1617/7 (DFG Research Group BioGeoChemistry of Tidal Flats).

Appendix A

To compose matrix eq 8, values of integral operators **G** and **H**

$$\mathbf{G}_{ij} = \iint_{\Gamma_j} G(\mathbf{r}, \mathbf{r}_i) d\Gamma \quad (19)$$

$$\mathbf{H}_{ij} = \begin{cases} \iint_{\Gamma_j} \frac{\partial G(\mathbf{r}, \mathbf{r}_i)}{\partial \mathbf{n}} d\Gamma, & i \neq j \\ \frac{1}{2} + \iint_{\Gamma_j} \frac{\partial G(\mathbf{r}, \mathbf{r}_i)}{\partial \mathbf{n}} d\Gamma, & i = j \end{cases} \quad (20)$$

must be calculated for all source points and all boundary elements. Whereas operator **H** has regular kernel and can be evaluated numerically for all combinations of indices *i* and *j* in eq 20, operator **G** has an irregular kernel for *i* = *j*

$$\mathbf{G}_{ii} = \iint_{\Gamma_i} G(\mathbf{r}, \mathbf{r}_i) d\Gamma \quad (21)$$

and must be calculated analytically because the Green's function is not defined in the source point preventing numerical calculation of **G** for *i* = *j*. Instead integration is performed analytically in the plane of boundary element *i* using radial coordinates, **r** = (*r*, φ). Using this coordinates eq 21 becomes

$$\mathbf{G}_{ii} = \int_0^{2\pi} \int_0^{R(\theta)} G(\mathbf{r}, \mathbf{r}_i) dr d\theta \quad (22)$$

Let *R*(θ) be the distance from the source point **r**_s at the element center to the element edge for $\varphi \in [0, 2\pi]$, as depicted in Figure 6. Then, integrating eqs 22 over *r* yields correspondingly

$$\mathbf{G}_{ii} = \frac{1}{4\pi} \int_0^{2\pi} R(\theta) d\theta \quad (23)$$

For integration over φ , the triangular element is divided into three parts Δ_1 , Δ_2 , and Δ_3 as shown in Figure A1b. This yields for the integral in eq 23

$$\mathbf{G}_{ii} = \frac{1}{4\pi} \sum_{k_{\Delta}=1}^3 R_{0,k_{\Delta}} \sin(\beta_{k_{\Delta}}) \left\{ \ln \left(\tan \frac{\alpha_{k_{\Delta}} + \beta_{k_{\Delta}}}{2} \right) - \ln \left(\tan \frac{\beta_{k_{\Delta}}}{2} \right) \right\} \quad (24)$$

Results of eq 24 are used in the BEMSolver to evaluate **G** values for *i* = *j*.

All other operators are calculated numerically using the Gauss–Legendre 13-point quadrature rules.

References and Notes

- (1) Scanning Electrochemical Microscopy; Bard, A. J., Mirkin, M. V., Eds.; Marcel Dekker: New York, Basel, 2001.
- (2) Barker, A. L.; Gonsalves, M.; Macpherson, J. V.; Slevin, C. J.; Unwin, P. R. *Anal. Chim. Acta* **1999**, *385*, 223.
- (3) Wittstock, G. Imaging Localized Reactivities of Surfaces by Scanning Electrochemical Microscopy. In *Solid–Liquid Interfaces, Macroscopic Phenomena – Microscopic Understanding*; Wandelt, K., Thurgate, S., Eds.; Springer-Verlag: Berlin, Heidelberg, 2003; pp 335–364.
- (4) Wittstock, G. *Fresenius J. Anal. Chem.* **2001**, *370*, 303.
- (5) Horrocks, B. R. Scanning Electrochemical Microscopy. In *Instrumentation and Electroanalytical Chemistry*; Unwin, P. R., Ed.; Wiley-VCH: Weinheim, 2003; Vol. 3; pp 444–490.
- (6) Kwak, J.; Bard, A. J. *Anal. Chem.* **1989**, *61*, 1221.
- (7) Unwin, P. R.; Bard, A. J. *J. Phys. Chem.* **1991**, *95*, 7814.
- (8) Bard, A. J.; Mirkin, M. V.; Unwin, P. R.; Wipf, D. O. *J. Phys. Chem.* **1992**, *96*, 1861.
- (9) Mirkin, M. V.; Bard, A. J. *J. Electroanal. Chem.* **1992**, *323*, 29.
- (10) Selzer, Y.; Mandler, D. *Anal. Chem.* **2000**, *72*, 2383.
- (11) Sklyar, O.; Wittstock, G. *J. Phys. Chem. B* **2002**, *106*, 7499.
- (12) Liljeroth, P.; Johans, C.; Slevin, C. J.; Quinn, B. M.; Kontturi, A.-K. *Anal. Chem.* **2002**, *74*, 1972.
- (13) Nann, T.; Heinze, J. *Electrochim. Acta* **2003**, *48*, 3975.
- (14) Martin, R. D.; Unwin, P. R. *J. Electroanal. Chem.* **1997**, *439*, 123.
- (15) Amphlett, J. L.; Denuault, G. *J. Phys. Chem. B* **1998**, *102*, 9946.
- (16) Nann, T.; Heinze, J. *Electrochem. Commun.* **1999**, *1*, 289.
- (17) Qiu, F. L.; Fisher, A. C. *Electrochem. Commun.* **2003**, *5*, 87.
- (18) Qiu, F. L.; Fisher, A. C. *Electrochem. Commun.* **2000**, *2*, 738.
- (19) Fulian, Q.; Williams, N. A.; Fisher, A. C. *Electrochem. Commun.* **1999**, *1*, 124.
- (20) Fulian, Q.; Fisher, A. C.; Denuault, G. *J. Phys. Chem. B* **1999**, *103*, 4393.
- (21) Fulian, Q.; Fisher, A. C.; Denuault, G. *J. Phys. Chem. B* **1999**, *103*, 4387.
- (22) Fulian, Q.; Fisher, A. C. *J. Phys. Chem. B* **1998**, *102*, 9647.
- (23) Sklyar, O.; Kueng, A.; Kranz, C.; Mizaikoff, B.; Lugstein, A.; Bertagnolli, E.; Wittstock, G. *Anal. Chem.* **2005**, *77*, 764.
- (24) Sklyar, O.; Ufheil, J.; Heinze, J.; Wittstock, G. *Electrochim. Acta* **2003**, *49*, 117.
- (25) Träuble, M.; Sklyar, O.; Wittstock, G. Boundary Element Simulation for Transient Measurement in SECM; International Conference on Boundary Element Techniques VI, 2005, Montreal, Canada.
- (26) Bard, A. J.; Fan, F.-R. F.; Mirkin, M. V. Scanning Electrochemical Microscopy. In *Electroanalytical Chemistry*; Bard, A. J., Ed.; Marcel Dekker: New York, Basel, Hong Kong, 1994; Vol 18.
- (27) White, H. S. *Electrochem. Soc. Interface* **2003**, *12*, 30.
- (28) Scott, E. R.; White, H. S.; Phipps, J. B. *Anal. Chem.* **1993**, *65*, 1537.
- (29) Zhao, C.; Sinha, J. K.; Wijayawardhana, C. A.; Wittstock, G. *J. Electroanal. Chem.* **2004**, *561*, 83.
- (30) Wijayawardhana, C. A.; Wittstock, G.; Halsall, H. B.; Heineman, W. R. *Anal. Chem.* **2000**, *72*, 333.
- (31) Wijayawardhana, C. A.; Wittstock, G.; Halsall, H. B.; Heineman, W. R. *Electroanalysis* **2000**, *12*, 640.
- (32) Wittstock, G.; Yu, K.-j.; Halsall, H. B.; Ridgway, T. H.; Heineman, W. R. *Anal. Chem.* **1995**, *67*, 3578.
- (33) Shiku, H.; Hara, Y.; Matsue, T.; Uchida, I.; Yamauchi, T. *J. Electroanal. Chem.* **1997**, *438*, 187.
- (34) Shiku, H.; Matsue, T.; Uchida, I. *Anal. Chem.* **1996**, *68*, 1276.
- (35) Torisawa, Y. S. Y.-S.; Shiku, H.; Yasukawa, T.; Nishizawa, M.; Matsue, T. *Biomaterials* **2005**, *26*, 2165.
- (36) Shiku, H.; Shiraishi, T.; Aoyagi, S.; Utsumi, Y.; Matsudaira, M.; Abe, H.; Hoshi, H.; Kasai, S.; Ohya, H.; Matsue, T. *Anal. Chim. Acta* **2004**, *522*, 51.
- (37) Kaya, T.; Numai, D.; Nagamine, K.; Aoyagi, S.; Shiku, H.; Matsue, T. *Analyst* **2004**, *129*, 529.
- (38) Yasukawa, T.; Kaya, T.; Matsue, T. *Chem. Lett.* **1999**, *9*, 975.
- (39) Tsionsky, M.; Cardon, Z. G.; Bard, A. J.; Jackson, R. B. *Plant Physiol.* **1997**, *113*, 895.
- (40) Bauermann, L. P.; Schuhmann, W.; Schulte, A. *Phys. Chem. Chem. Phys.* **2004**, *6*, 4003.
- (41) Hengstenberg, A.; Blöchl, A.; Dietzel, I. D.; Schuhmann, W. *Angew. Chem., Int. Ed.* **2001**, *40*, 905.
- (42) Serebrennikova, I.; White, H. S. *Electrochem. Solid State. Lett.* **2001**, *4*, 4.
- (43) Basame, S. B.; White, H. S. *Langmuir* **1999**, *15*, 819.
- (44) Basame, S. B.; White, H. S. *J. Phys. Chem. B* **1998**, *102*, 9812.
- (45) Basame, S. B.; White, H. S. *J. Phys. Chem.* **1995**, *99*, 16430.
- (46) Casillas, N.; Charlebois, S. J.; Smyrl, W. H.; White, H. S. *J. Electrochem. Soc.* **1994**, *141*, 636.
- (47) Engstrom, R. C.; Meaney, T.; Tople, R.; Wightman, R. M. *Anal. Chem.* **1987**, *59*, 2005.
- (48) Mauzeroll, J.; Hueske, E. A.; Bard, A. J. *Anal. Chem.* **2003**, *75*, 3880.
- (49) Scott, E. R.; White, H. S.; Phipps, J. B. *J. Membr. Sci.* **1991**, *58*, 71.
- (50) Zhao, C.; Wittstock, G. *Biosens. Bioelectron.* **2005**, *20*, 1277.
- (51) Macpherson, J. V.; Unwin, P. R. *J. Phys. Chem.* **1995**, *99*, 14824.
- (52) Barker, A. L.; Unwin, P. R.; Zhang, J. *Electrochem. Commun.* **2001**, *3*, 372.
- (53) Barker, A. L.; Unwin, P. R. *J. Phys. Chem. B* **2001**, *105*, 12019.
- (54) Barker, A. L.; Unwin, P. R.; Amemiya, S.; Zhou, J.; Bard, A. J. *J. Phys. Chem. B* **1999**, *103*, 7260.
- (55) Martin, R. D.; Unwin, P. R. *Anal. Chem.* **1998**, *70*, 276.
- (56) Martin, R. D.; Unwin, P. R. *J. Chem. Soc., Faraday Trans.* **1998**, *94*, 753.
- (57) Wittstock, G.; Asmus, T.; Wilhelm, T. *Fresenius J. Anal. Chem.* **2000**, *367*, 346.

- (58) Sklyar, O.; Treutler, T. H.; Vlachopoulos, N.; Wittstock, G. *Surf. Sci.* **2005**, *597*, 181.
- (59) Wijayawardhana, C. A.; Ronkainen-Matsuno, N. J.; Farrel, S. M.; Wittstock, G.; Halsall, H. B.; Heineman, W. R. *Anal. Sci.* **2001**, *17*, 535.
- (60) Invitrogen, <http://www.invitrogen.com/content.cfm?pageid=11049>
- (61) Nowall, W. B.; Dontha, N.; Kuhr, W. G. *Biosens. Bioelectron.* **1998**, *13*, 1237.
- (62) Strike, D. J.; Hengstenberg, A.; Quinto, M.; Kurzawa, C.; Koudelka-Hep, M.; Schuhmann, W. *Microchim. Acta* **1999**, *131*, 47.
- (63) Zhao, C.; Wittstock, G. *Anal. Chem.* **2004**, *76*, 3145.